THE BEAGLE 2 STEREO CAMERA SYSTEM

A. D. Griffiths[a,*], A. J. Coates[a], J.-L. Josset[b], G. Paar[c], B. Hofmann[d], D. Pullan[e], P. Rüffer[f], M.R. Sims[e] and C.T. Pillinger[g]

[a]Mullard Space Science Laboratory, University College London, Holmbury St. Mary, Dorking, RH5 6NT, UK
[b]Space-X, Jaquet-Droz 1, CH-2007 Neuchâtel, Switzerland
[c]Institute of Digital Image Processing, Joanneum Research, Wastiangasse 6A- 8010, Graz, Austria
[d]Natural History Museum, Bern, Switzerland
[e]Dept. of Physics and Astronomy, University of Leicester, Leicester, UK.
[f]Institut für Datentechnik und Kommunikationsnetze der TU Braunschweig, Braunschweig, Germany
[g]Dept. of Earth and Planetary Sciences, OpenUniversity, Milton Keynes, U.K.

Proofs should be sent to:
Mullard Space Science Laboratory, University College London, Holmbury St. Mary, Dorking, RH5 6NT, UK

Requests for offset prints should be sent to Dr. A. D. Griffiths,

*Corresponding Author: A.D. Griffiths
Fax: +44 (0) 1483 278312, email: adg@mssl.ucl.ac.uk

Abstract

The Stereo Camera System (SCS) was designed to provide wide-angle multi-spectral stereo imaging of the Beagle 2 landing site. Based on the Space-X micro-cameras, the primary objective was to construct a digital elevation model of the area in reach of the lander's robot arm. The SCS technical specifications and scientific objectives are described; these included panoramic 3-colour imaging to characterise the landing site; multi-spectral imaging to study the mineralogy of rocks and soils beyond the reach of the arm and solar observations to measure water vapour absorption and the atmospheric dust optical density. Also envisaged were stellar observations to determine the lander location and orientation, multi-spectral observations of Phobos & Deimos and observations of the landing site to monitor temporal changes.

1. Introduction

The Stereo Camera System (SCS) provided the primary imaging capability of the Beagle 2 Mars lander (Sims et al., 1999, 2000). The 'micro camera modules' that form the heart of the system were developed over some 10 years by the Swiss co-investigators, Space-X. This development work succeeded in producing a lightweight, rugged camera for space applications, which was subsequently made available to the Beagle 2 project (Josset, & Beauvivre, 2003). A similar Space-X camera system, AMIE is currently flying on the ESA SMART-1 spacecraft.

Due to the unique nature of the Beagle 2 mission, the SCS design and development process was unusually compressed. Starting in January 2000 with the cameras and the basic filter wheel design, a compressed assembly, integration and verification programme was initiated. Both development and flight model (DM and FM respectively) versions of SCS were built – although only one micro camera module was available to the DM. The DM was used for qualification level environmental testing (thermal, shock and vibration) at instrument level. Having survived this qualification it went on to become the ground reference model of the SCS and was integrated into the PAW (position adjustable workbench) of the corresponding Beagle 2 ground test model. In addition to PAW sub-system level environmental qualification, the FM SCS was subject to a geometric and radiometric calibration programme before delivery to the FM PAW. Integration of the flight model onto the Beagle 2 PAW occurred in November 2002. Further PAW and lander integration and verification then cumulated with the delivery of the Beagle 2 lander to the Baikonur launch site on March 20th, 2003.

Launched along with the ESA Mars Express orbiter on June 2nd, 2003, Beagle 2 separated as planned on 19th December 2003 for a five-day ballistic coast to Mars. Unfortunately, Beagle 2 never made contact after the anticipated touch down in Isidis Planitia on 25th December 2003 and was subsequently declared lost.

In this paper, we discuss the unique miniaturized design of the SCS and the outline the scientific and lander engineering-related objectives of this imaging system. The Stereo Camera System is described in detail in section 2 below, along with the rationale for filter selection in section 3. The DEM generation process is

described in section 4 and the basic camera calibration performed prior to launch is discussed in section 5. The primary science and engineering objectives are discussed in section 6 followed by our conclusions. The full SCS calibration programme and detailed system performance will form the basis of a future paper.

2. Stereo Camera System Technical Description

At 33%, Beagle 2 had the highest payload to support mass ratio of any planetary lander to date – i.e. 9 kg of payload plus 2 kg for the PAW and robot arm out of the 33.2 kg surface landed mass (Pillinger et al., 2003). Therefore, minimising component mass was a major priority during design and assembly. The final FM SCS total system mass of 360 g compares very favourably with other imagers sent to Martian surface (e.g. Bell et al., 2003 and Smith et al., 1997a), as does the 520 cm^3 volume envelope and 1.8 W average power consumption.

The Stereo Cameras were part of Beagle 2's highly integrated instrument complex known as the PAW, which was attached to the end of the 0.7 m long robot arm. The PAW provides mounting points for the twin camera/filter wheel units or "eyes", such that the stereo baseline is 209 mm between the CCD centroids, with the toe-in (or "cross eye" effect) fixed at 3.7° per eye. The 5 degree of freedom robot arm orientates the cameras to point in any required direction, from within the 0.7 m radius hemisphere above the lander base.

The arm is also used to position and orientate the other PAW contact instruments (Sims et al., 2003): i.e. PLUTO (the Planetary Underground Tool, also known as the 'Mole'), the Mössbauer and X-ray fluorescence spectrometers, the Microscope, the Rock Corer-Grinder (RCG) and the wind sensor from the Environmental Sensor Suite (ESS). The mole and the RCG are both capable of recovering soil and/or rock samples for chemical analysis by the Gas Analysis Package (GAP) mounted in the lander base (Morgan et al., 2003).

The SCS was designed, developed and integrated by UCL's Mullard Space Science Laboratory (MSSL).

Each SCS eye consisted of a Space-X CCD micro-camera with 48° optics and a MSSL filter wheel with twelve interference-coated filters. All the optics and filters were composed of anti-reflection coated radiation hard BK7 silica glass. The 10 mm (usable) diameter filters were mounted in a 59 mm diameter titanium filter wheel and protected from the dusty Martian environment by an aluminium housing and lid. A 15 mm diameter optical window in the lid allowed light to pass through to the filter wheel, which was rotated by a stepper motor and gear wheel assembly. A stainless steel "wiper blade" attached to the central gear shaft was provided to remove dust from the optical window (see figures 1 & 2).

The micro-camera module was based around a 1024 x 1024 pixel, frame transfer CCD device sensitive to visible and near infrared (IR) wavelengths between 400–1000 nm (see table 1 for the CCD performance characteristics). The wide-angle optics (table 2) and a choice of 24 filters allowed a wide range of scientific objectives to be addressed (tables 3 and 4).

The CCD and its supporting 10 bit analogue to digital (A/D) converter and 8 Megabyte memory; the interface, clocking and driver electronics were all arranged in a three dimensional stack of circuit boards and encapsulated to form a gold coloured block (53 mm along the maximum dimension). Hence, the micro-camera was a self-contained camera unit (and not merely a CCD detector) that communicated with the lander electronics via a 10 Mbit/s serial interface.

The micro-camera module was controlled by a five-byte command frame, which included the 16-bit integration time (i.e. 1–65535 ms selectable in steps of 1 ms). Another camera hardware control option was the ability to select between image data or control pixels (light shielded pixels surrounding the CCD active image area). Once an image had been acquired, it was transferred to the spacecraft mass memory and (optionally) compressed by the lander software using a lossy wavelet-encoding scheme (Rueffer & Borrmann, 2003) before transmission to Earth.

Since the SCS was designed to be fully exposed to the Martian thermal environment and no electrical power could be spared for heaters, the instrument temperatures would tend to follow the Martian

5

atmospheric temperature. Such low temperatures were not an operational or safety constraint as the SCS had been operated down to –150°C during instrument verification. However, accurate knowledge of the CCD operating temperature was required to estimate the dark current level in each image, since telemetry bandwidth constraints would have precluded the routine acquisition of dark images during the mission. Since the focal plane temperature sensor output could not be supported by the Beagle 2 PAW electronics due to an insufficient number of multiplexer channels, an external AD590 temperature sensor was attached to each micro-camera instead. The output from this sensor was cross-calibrated with focal plane temperature sensor during pre-launch instrument calibration.

The 48° field of view of the optics supplied with the Space-X micro camera complicated the SCS design (see table 2 for details of the 48° optics' performance). In addition to producing a circular illumination pattern that does not completely enclose the CCD (leaving the corners unilluminated – e.g. figure 3), due to the depth of focus available two working distances were required. The 48° optics were naturally optimised for viewing high priority objects within reach of the lander's robot arm – i.e. best focus between 0.6 and 1.2 m (see for example figure 3). To view objects at greater distances four filters with a lenticular cross-section (filters L8 and R8 to R10 in table 3) were used to provide the necessary optical accommodation. When using these four filters the best focus range was between 1.2 m and infinity. Additionally the R1 filter position contained a "close-up" lens (or CUL) to provide a magnified view of rock surface textures (similar to that provided by a geologist's hand lens). The CUL had 60 micron per pixel resolution at the 80 mm working distance (see figure 4 and table 3).

The filter wheel was attached to a gear wheel driven by a pinion gear on the stepper motor shaft. This design produced a one-filter position shift (equivalent to 30°) for every ten motor steps. The filter wheel was constrained by end stops to rotate a maximum of 330° (110 motor steps) clockwise or anticlockwise – which allowed all twelve filters to pass in front of the camera optics. A home position (filter position #12 – table 3) was defined by one end stop. Filters were then selected by counting motor steps from this home position. To simplify commanding each image sequence started and ended by driving the filter wheel back to the home position. The design did not therefore require electronic position sensing.

Additionally, a wiper blade was located between and above positions #1 & #2, such that selecting filter position #1 caused the wiper to move across the window sweeping away any accumulated dust. Ground testing with a spare filter housing showed no tendency for JSC Mars-1 regolith stimulant or Arizona road dust to scratch the window surface after nominal lifetime sweep testing (Griffiths et al., 2002).

Three other Beagle 2 components enhanced the effectiveness of the stereo cameras; these were the Wide-Angle Mirror (WAM), the two torches and the calibration target. Both the WAM and torches were suggested and developed by the University of Leicester PAW team (Sims et al., 2003), while the calibration target (in the form of a spot painting mounted on the lander body) was provided by the British artist Damien Hirst as part of the Beagle 2 public outreach programme (Pillinger et al., 2003).

The purpose of the wide-angle mirror was to view the surface of Mars before the PAW was deployed from the lander (at which point the cameras are staring straight up at the sky). It also served as a low mass alternative to the originally envisaged wide-angle camera and would have been used to observe mole deployment, retraction and surface operations. Once the lander lid had opened, the WAM would rotate to a position 80 mm above the top surface of the PAW (over the right eye). The mirror then provides a distorted view of the 360° panorama around the lander base (see figure 5 for an example image acquired during lander verification). The mirror surface had a parabolic form to maximise the amount of lander and Martian surface/sky that could be viewed by the camera (43% and 57% of the image respectively).

The torches provided a known spectrum of light to enable the stereo cameras to produce a true colour image of the Martian surface. These images must be acquired at night as the dust in the Martian atmosphere preferentially scatters the red component of sunlight producing a variable colour cast during the day (Thomas et al., 1999). The torches consisted of three high efficiency white light LEDs mounted together at the side of each filter wheel housing (see figure 1) to ensure maximum light flux in the field of view of that camera. The spectral output of these LEDs is reproduced from the manufacturer's data sheet in figure 6.

Although, prior to landing it was not possible to fully test the effectiveness of the torch we did manage to establish limits on the size and distance of the area that might be imaged. A ground test image using the CUL and right hand torch shows a approximately 460 pixel diameter saturated zone centred at CCD column 173 and row 220 with an exponential brightness decay beyond that (1 e-folding distance of 260 pixels). At the nominal working distance of 80 mm the saturated zone is approximately 29 mm in diameter with a cone angle of ~20°.

The Beagle 2 calibration target was a triangular aluminium surface with circular depressions containing 16 different mineral pigments, which were used to provide calibration samples for both the SCS and the PAW mounted spectrometers. Observations of this calibration target would have been made early in the mission before the ubiquitous air fall dust had time to accumulate. Comparison of daytime images and night time observations of the target illuminated with the torch would have provided data to better define the amount of reddening of direct and scattered sunlight by atmospheric dust. Armed with better information on the colour properties of the daytime illumination we hoped to create images of the surface as seen by a human eye on Mars and of rocks and soil as they would appear if view under terrestrial illumination conditions.

3. Filter Design and Pass Band Selection

The designed of the SCS 24-filter set reused many of the Imager for Mars Pathfinder filter wavelengths (see Smith et al., 1997a,b and the rational in section 6). However, since duplicating the Pathfinder filter set at two focusing distances would require 48 filters, an process of optimisation took place as we attempted to find the best possible set of wavelengths to achieve the science goals, with the minimum number of filter positions.

For example, although there is some overlap between the centre wavelengths of interest for both the geology and the solar imaging it is not possible to use one set of filters for both. If the sun were observed through the geology filters the detector would saturate in much less than the minimum possible integration time of 1 ms. Instead, the solar filters had an extra metallic coating (providing a neutral density filter with

an optical density of approximately 5) and narrower 5-6 nm pass bands to limit the amount of light reaching the detector. This allowed solar filter integration times of 15-20 ms and minimised the image-smearing problem that occurs for integrations close to the 2 ms frame transfer time[1]. A narrow band pass is also required to accurately measure the absorption in the 5 nm wide 935 nm water vapour band. Hence, in addition to the 12 geology filter wavelengths, a further 6 solar filters were chosen.

Team members Joanneum Research (of Graz, Austria) advised that monochromatic stereo imaging, at any stereo filter wavelength > 600 nm, was sufficient for production of the mission critical DEM. Hence, a 670 nm central wavelength was chosen so that the same filters could provided the stereo and red-channel images. Since 670 nm was considered sufficient for DEM imaging, the Pathfinder 970 nm high contrast stereo pair was not selected, saving two filter wheel positions.

In addition to two pairs of 670nm stereo filters (for the near and far focus range), the short focal range geology filters at 440, 530 nm on the left eye allowed the acquisition of red-green-blue (RGB) colour composites. Therefore, a further two lenticular filters (at 440, 530 nm on the right eye) were required to provide RGB colour imaging in the far focus range.

Filters with the same science objectives were grouped together on each wheel to minimize the rotational movement required to acquire an image sequence (and therefore over all wear-and-tear). When not using the cameras the filter wheels would be parked in the home positions (L12 & R12), which contain long wavelength solar filters to minimise exposure of the CCD to UV light during daytime. The final SCS filter set including the CUL is summarised in table 3.

4. Digital Elevation Models

Generation of a landing site DEM to support PAW science activities was the primary design goal for the SCS. Given that the light time delay between Earth and Mars is always > 4 minutes, manual remote control

---

[1] E.g. the last row of the 2 ms integration would actually be exposed to light for 4 ms – twice as long as the first row read out

of the robot arm was not possible. Hence, an accurate DEM was vital to avoid surface collisions during pre-programmed arm movements and to allow initial positioning of the PAW instruments in close proximity to rock and soil surfaces.

Mission planning called for the DEM and the lander CAD model to be incorporated into a VR model of the landing site. The DEM data would also be used to create a "rapid prototype" physical model of the landing site to be incorporated into the Beagle 2 Ground Test Model (GTM). Both these simulation facilities would have been used sequentially to generate and validate the arm and PAW command sequences during day-to-day operations planning before uplink to the Beagle 2 FM. Although no data was ever received from Beagle 2 on Mars, the above operation scenarios were fully tested using the GTM, during the cruise phase of the mission.

The DEM was generated by merging a set of overlapping individual stereo-pairs. The orientation and geometrical distortion of each individual stereo pair would be known from the robot arm joint angle telemetry in combination with a head-eye calibration of the cameras on the PAW (Barnes et al., 2002 and 2003). After the images were received on the ground, they would be ingested into a geometric calibration software suite where lens distortion correction, stereo matching, DEM reconstruction and global adjustments would be applied. This process would yield a DEM around the lander free from artefacts in the borders between its individual component views. The integrity of the DEM and its accuracy with respect to the lander co-ordinate system would have been evaluated during the mission by observing parts of the lander frame within the field of view of the cameras. These lander features could be integrated with the DEM because the camera viewing parameters, along with a full dynamic CAD model of the lander and robot arm were available.

Pre-flight internal optical and external inter-eye calibration was performed with both the DM and FM camera and PAW models by imaging carefully designed calibration targets and surveying the camera-PAW-target geometry with a theodolite (ibid). During this PAW-arm verification DEM accuracy was calculated to be within 3 mm in the x, y and z-axes (Barnes et al., 2003) for camera to target surface

distances of approximately 1m. This translated to a repositioning accuracy of not greater than 5 mm for any of the PAW tool tips on a given rock in the DEM. The effectiveness of this calibration was demonstrated shortly before landing by using the Envision™ data to program the Beagle 2 GTM mole to acquire a sample of soil stimulant and deliver it to the GAP inlet.

As the accuracy of the reconstruction is proportional to the stereo baseline and inversely proportional to a quadratic function of range (Paar et al., 1999), there would inevitably be loss of accuracy in the DEM at larger distances from the lander (i.e. a 6 mm error at 1m distance grows to a c.a. 60 cm error at 10 m). Additionally, the low viewing angles would result in obscuration of background features by foreground objects. These effects might have been reduced later in the mission by using the range of travel of the robot arm to increase the stereo baseline between a pair of images acquired with the same camera. However, our knowledge of the accuracy of the stereo separation and viewing angles would be lower than for the properly calibrated stereo pair, leading to larger position errors in the resulting DEM.

Joanneum Research provided the expertise and software for camera stereo calibration, DEM generation, image mosaicking and WAM unwrapping to produce panoramas. The space robotics group of the University of Aberystwyth (in Wales) were able to input the SCS DEMs into a VR simulation of the lander and its surroundings using the ENVISION™ software. Both groups collaborated to geometrically calibrate the SCS-PAW-arm system (Barnes et al., 2002 and 2003).

5. Basic Calibration Programme and Results

Although SCS development and flight models (DM & FM respectively) were constructed, only the FM eyes underwent both a radiometric and geometric calibration (see section 4) programme prior to launch. In addition to understanding the instrument behaviour, it was also necessary for accurate image data calibration to be able to predict parameters (like dark current) that could not be routinely transmitted back to Earth. The radiometric calibration was conducted at six different temperatures of –100°C, –60°C, –30°C,

–10°C, +5°C and +20°C in a vacuum dewar. We attempted to acquire data over the full range of temperatures expected to be encountered on Mars but did not seek to duplicate the Martian atmospheric pressure or chemical composition in the dewar.

Initial tests were conducted in darkness (by placing a light proof cover over the dewar window) to determine the CCD bias current and magnitude of the dark current. Later tests using an incandescent tungsten source examined the SCS system spectral response, modulation transfer function, flat field properties and the CCD transfer curve. The power spectrum of this source was determined with a spectral-radiometer, to an accuracy of 1.5 % (the lamp was allowed to reach it's steady state operating temperature before use).

5.1 Bias Current

The bias current is an analogue offset applied to the CCD readout to prevent the A/D converter input going negative due to electrical noise. Although small, it should be determined to achieve maximum radiometric accuracy. Bias current measurements were made by acquiring minimum integration time (i.e. 1 ms) images with each FM eye at the six temperatures of interest. This ensured that the contribution from dark current noise was minimised – however, due to the 2 ms frame transfer time some noise gradient between the first and last rows read out was unavoidable.

To remove random noise median bias images, for each eye at each temperature, were assembled by taking the median value of each pixel position in the nine raw bias images. The resulting composite images were examined for fixed pattern noise and a signal was detected – apparently due to the micro-camera onboard clock. The mean pixel value (of the entire image) showed a slight increase over the –100 to +20°C range but stayed within 14±1 DN^2 for the left eye and 19±1 DN for the right. Actual pixel values varied by less than ±5 DN of these values for all the bias images, with the histogram widths generally increasing with temperature to this figure at +20°C.

---

[2] DN = digital number – i.e. a brightness unit equal to 2^{-10} (due to the 10-bit A/D converter) of the saturated CCD output.

5.2 Dark current

Dark current images were acquired by taking maximum length integrations (of 65.535 s) in darkness. Like the bias current images, multiple frames were acquired for each FM at each of the six temperatures. These images were combined to produce a median dark current image at each temperature and then the matching median bias image was subtracted.

The median dark current images were inspected for cosmetic defects and hot pixels (defined as deviating by $>\pm5\sigma$ of the image mean) and found to exhibit very little dark current pixel-to-pixel non-uniformity. Only some one to two hundred deviant pixels were counted (approximately 0.02% of the array) on each CCD – most of which were dark current related as the number increased rapidly with temperature at –10°C and above. However, only a single pixel (at column 74, row 159) on the left eye was above 5σ of the image mean at all six temperatures. Similarly a single pixel (at position 1023,1023) on both CCDs was observed to be consistently stuck at 0 DN.

Finally for each CCD the median noise in a square 1600 pixel region at the centre of each median image was calculated and fitted to the dark current relation of Janesick (2001):

$$\bar{I}_{DC} = 2.5\times10^{15} P_s D_{fm} T^{1.5} e^{\left(-E_g/2kT\right)}$$
(1)

Where: $\bar{I}_{DC}$ = the mean dark current (e⁻/pixel/s), P_s= the pixel area = 1.96x10⁻⁶ cm², D_{fm}= the dark figure of merit (nA/cm²), T= the CCD temperature (K), E_g= the silicon band gap (eV) = $1.1557–7.021\times10^{-4}.T^2/(1108+T)$ and k= Boltzmann's constant (8.62x10⁻⁵ eV/K). The fits allowed the dark figure of merit parameter D_{fm} to be derived for each CCD (see table 1).

5.3 Pixel Non-uniformity

Using an integrating sphere to uniformly distribute light from the source onto each SCS eye, a set of five flat field images was acquired for the majority of filters at -30°C. Unfortunately, the solar filter transmission was too low to produce usable images when viewing light from the source scattered via

integrating sphere). For each of the non-solar filters these images were combined into a median flat field image (in the same manor as the bias and dark images). The other temperature points were not considered to save time during calibration, as (after accounting for thermal dark current) the pixel-to-pixel non-uniformity was not expected to be a strong function of temperature.

Apart from the unilluminated corners due to vignetting by the SCS 48° optics, the flat field images are very uniform visually but clearly show an 18–20% radial brightness fall-off (an expected characteristic of imaging systems, i.e. Smith et al., 1997a). This fall-off can be fitted by a quadratic function of radius and is slightly offset from the CCD geometric centre for each eye, due to the tolerance on the alignment of the lens optical axis off of normal to the CCD image plane. The exceptions to this rule are the L1 and L2 filters which show a pattern of annular bands, apparently due to a manufacturing defect. These flat field properties made it more difficult to quantify the pixel-to-pixel non-uniformity but for the square central 1600 pixel region of each CCD the standard deviation on the mean brightness is 0.5–1.1%.

5.4 CCD Transfer Curve

The flat field images were also used to plot the CCD transfer curve and measure the CCD linearity. The CCD transfer curve (figure 7) is a plot of pixel value versus the associated pixel variance assembled from images acquired with several different integration times. The inverse slope of the plot gives the system gain and the y-axis intercept provides a measure of the read-out noise (see table 1). The CCD full well values in table 1 are calculated by multiplying the system gains by the ADC full well output of 1023 DN.

This procedure yielded values for the read-out noise of 0.37±0.03 and 0.39±0.03 DN for the left & right eyes respectively. These results compare favourably with less precise (maximum) values of 0.46±0.14 and 0.48±0.19 (respectively), calculated from the standard deviations of the "stacks" of nine pixels from each of the raw images that were combined to produce the median bias images.

5.5 CCD Linearity

The linearity of the CCD was measured by plotting the CCD response in DN against the integration time

14

(figure 8). Both CCDs were confirmed to be highly linear in the measured range (0–950 and 0–600 DN for the left & right eyes respectively) with correlation coefficients in the range 0.9999–1.0. Due to the different count rates of the two CCDs of 1201 and 910 DN/s for the left & right eyes respectively (figure 8) the pre-calculated integration times did not cover the full dynamic range of the right eye CCD. As the same source was used for both eyes, the 24% difference in count rates is surprising. However, it maybe partly explained by the (unquantified) effect of the software selectable (4 bit) PGA gain register being set at 11 and 12 (for the left & right eyes respectively), as recommended by the Space-X for normal operations.

5.6 Estimated CCD Quantum Efficiency and System Responsivity

Due to the limited time available before launch, it was not possible to accurately measure the FM SCS CCD Quantum Efficiency (QE). Instead post-launch measurements were made on one of the DM eyes. These measurements were shown to agree tolerably well with the manufacturer's published quantum efficiency (only available at 25°C – see figure 9). Therefore, the manufacturer's QE measurement was used to derive the approximate system responsivity discussed below.

The SCS system responsivity or sensitivity of the camera was calculated from the relationship presented by Maki et al. (1999) – reproduced here as equation 2.

$$R(\lambda) = A\Omega\delta\lambda T_{filter}(\lambda)\frac{QE(\lambda)}{gain}\cdot\frac{\lambda}{hc} \tag{2}$$

Where: $R(\lambda)$= the system responsivity in units of (DN/s)/[W/(m^2.st.μm)], A= the detector pixel area = 1.96×10^{-10} m^2, Ω= the solid angle subtended by the aperture at the pixel (0.038 steradians), $\delta\lambda$= the system spectral bandpass (μm), $T_{filter}(\lambda)$= the optics and filter bandpass transmission (%), $QE(\lambda)$= the (manufacturers) quantum efficiency (%), $gain$= the CCD gain (see table 1) in e$^-$/DN, λ= the filter central wavelength (m), h= Plank's constant (6.626 $\times10^{-34}$ J.s) and c= the speed of light (2.998×10^8 m/s).

Calculated responsivities for all 24 filters are given in table 5 along with the CCD manufacturer QE (only available at 25°C) and filter-lens transmission factors. Figure 10 shows a graphical comparison of the responsivities of the SCS and two recent Mars surface imagers. The SCS responsivities compare well with

those of the Mars Exploration Rover PanCam filters, being within a factor of 0.7 to 3.6 less than the equivalent filter central wavelength (Bell et al., 2003). They are also seen to be between a factor of 3.5 and 10 less than that of equivalent Mars Surface Stereo Imager filters (part of the MVACS payload on the ill-fated Mars Polar lander – Smith et al., 2001).

5.7 Signal to Noise Ratio

The signal to noise ratio (SNR) of a CCD image can be defined as the desired signal value divided by the quadrature sum of the relevant noise terms (the square root of the sum of the squared terms). In equation 3 the photon (shot) noise, dark current and read noise terms are used to calculate the pixel SNR.

$$SNR = \frac{P.QE.t}{\sqrt{(P+B).QE.t + D_n t + N_r{}^2}} \tag{3}$$

Where: P= the signal photon flux (photons/pixel/s), B= the background (e.g. scattered light) flux reaching the CCD (photons/pixel/s), QE= the quantum efficiency (%), t= the integration time (s), D_n= the dark current (electrons/pixel/s), N_r= the read out noise (RMS electrons/pixel).

Figure 11 shows calculated SNR versus wavelength for the left and right eyes at 25 °C. Again use was made of the manufacturer's QE data and assuming a maximum signal level of 800 DN (plus 5% scattered background light) after a 10 second integration. Wavelength averaged SNR under these conditions for the left and right eyes are shown in table 1. The lower right eye values are predominantly due to its lower gain (table 1).

5.8 Image Quality

The system image quality was tested by imaging a 21 micron diameter slit (oriented horizontally, vertically or at ±45° relative to the image plane) with the lenticular and plane parallel RGB colour filters, the solar filters and the CUL. Images were acquired at -30°C for the left eye and erroneously, at 0°C for the right. Due to our tight schedule, camera-slit separations were chosen to be close to the near edge of the two SCS focusing ranges where performance was expected to be poorest (i.e. 0.68 m for plane parallel filters, 1.32 m for lenticular filters and 79 mm for the CUL) to define a lower limit. Note that the slit is unresolved at all

16

three distances – equivalent to pixel scales of 510, 990 and 60 microns for the plane parallel filters, lenticular filters and CUL respectively). These images were processed to provide line spread profiles across the slit, which were then Fourier transformed to yield the Modulation Transfer Function (MTF). Unfortunately a common slit orientation was not used for both eyes; hence for maximum compatibility vertical slit images were used to generate all left eye MTF curves and diagonal slit images were used for the right eye. Note: the difference in slit orientation does not noticeably affect the MTF curves for the 670 nm L7 filter where both vertical and diagonal slit images were acquired (see figure 12b).

For example, figure 12a is a plot of brightness profiles across three images of a 21 micron width slit acquired with the Left eye L7 filter. The three perpendicular profiles are for the slit oriented horizontally, vertically and diagonally (45°) to the CCD pixel row structure. Integrating the vertical, horizontal and diagonal brightness profiles (after subtracting the average noise level) shows that in all three cases 95% of the transmitted energy lies within ±2 pixels of the peak.

For ideal diffraction limited systems, MTF values decrease with increasing photon wavelength for any given spatial frequency, while the MTF curves for different wavelengths diverge with increasing spatial frequency (being normalised to 100% at zero spatial frequency). Each SCS MTF profile (figure 13) falls monotonically to the Nyquist spatial frequency[3], indicating the expected fall in transferred image contrast with increasing spatial frequency. However, the expected behaviour at different photon wavelengths is not seen due to variations in slope of each SCS MTF curve. Taking for example the plane parallel filters on the left eye, over most of the 0 to Nyquist spatial frequency range the 670 nm (not the 440 nm) filter has the highest MTF values and the 880 nm (not the 990nm) filter has the lowest values. For these filters at the Nyquist frequency, MTF values are (in decreasing order) 39% for the 990 nm filter, 35% for the 670 nm filter, 32% for the 440 nm filter and 16% for the 880 nm filter.

A similar pattern is seen for the lenticular 440 nm and 670 nm filters on the right eye, which are both well below the equivalent left eye filters. The poorer MTF performance of the right eye 440nm and 670 nm

---

[3] A Nyquist frequency of 35.71 mm^{-1} is defined by the 14 micron SCS pixel pitch.

filters compared to those on the left indicates that either their precise position along the optical axis or their lenticular figure is not optimally matched to optical characteristics of the 48° lens at the near end of their working range. Unfortunately no right eye slit images were acquired at greater distances to allow the lenticular filter performance at infinity to be accessed.

The poor performance of the 440 nm filters on each eye (compared to the 670 nm filters) correlates well with their poor maximum transmission (table 5) and may be linked to radial variations in the left 440 nm transmission noted in the flat field images. No such transmission variation was seen in the other geology filters. The unexpected reversal of the MTF values of the left eye 880 and 990 nm filters is harder to understand. However, as these are both solar filters, small variations in coating thickness in the metallic neutral density layer or some form of surface contamination may be responsible for degrading the performance of the 880 nm filter.

Finally, a pair of ghost images (displaced slightly from the main image) was noted in 9 out of the 11 filter images used for MTF measurements. For the left eye images only the brightest ghost with an average intensity of 6.5±0.7% of the main image could be accurately measured, as the other more displaced ghost image was too close to the noise level. In the CUL images both ghosts were measured with an average intensity of 15.1±1.4% and 13.7±6.1% of the main image. In contrast, no ghosts were detected in the R8 and R9 colour lenticular filters.

5.9 SCS Image Calibration Software Pipeline

We planned that the Beagle 2 image telemetry packets would be automatically unpacked upon reception and assembled into raw 10-bit image data files, which would then be presented to the SCS team for processing, calibration and analysis. The first step in this chain was to run a bespoke utility to convert each of the storage efficient 10-bit pixels in the image into more computationally efficient 16-bit words. Software was written (using the Interactive Data Language™) to ingest these 16-bit files and if necessary decompress the image (image compression and decompression utilised the lossy wavelet transform described by Rueffer & Borrmann, 2003). The image processing software would then allow the user to

process and calibrate flight images by minimising CCD artefacts and noise – and (optionally) to perform a radiometric calibration. The software automatically acquired the relevant image temperature, integration time, eye and filter position parameters from the raw image file name. This data was then preserved in the (SCS specific) file header when the processed image was saved in 16-bit Tagged Image File Format (TIFF).

The geometric calibration (section 5.9 and Barns et al., 2003) was not included in the image processing software, as the distortions were deemed too small to noticeably degrade the data quality of individual images. For DEM and panoramic images, these geometric corrections were applied by a separate software suite written and operated by Joanneum Research.

A library of ground calibration images was assembled based on the FM calibration data (including median bias, dark current and flat field images). The software was designed to interpolate these median bias and dark current images to the temperature at which the flight image had been acquired. These images would then be subtracted from the flight image to reduce the image noise floor and remove the fixed pattern noise in the bias current. Finally, the new image would be divided by the appropriate (combined CCD and filter) flat field to minimise pixel-to-pixel non-uniformity.

The resulting 16-bit TIFF and derived 8-bit images would have been feed into a database for mission operations and public relations purposes. After the mission the images would have been processed further to allow their incorporation into the ESA planetary data archive (compatible with the NASA planetary data system data archiving conventions). For the more detailed scientific investigations described in section 6 below, the software also provided an option to implemented the radiometric calibration of the image (producing a floating point format data file) using the method described in section 5.6.

6. Scientific Objectives

A wide range of scientific objectives are possible using the visible and near IR spectral response of the SCS

system, based on the Space-X micro-camera. MSSL's primary scientific interest to be performed in conjunction with Mars Express ASPERA was the loss of water from the Martian atmosphere to space. It was recognised early in the design process that the SCS was capable of performing investigations similar to those of the Imager for Mars Pathfinder (IMP – Smith et al., 1997a,b), while the torch and close-up lens provide additional capabilities. In early 2000 the SCS team consulted with UK-based experts in planetary geology and determined that the IMP geology filter set was still the most appropriate choice for a Mars lander imager. Furthermore, we believed that there would be a strong synergy in observing at similar wavelengths at the two widely separated landing sites – i.e. IMP at Ares Vallis and the SCS at Isidis Planitia.

Beagle 2 was a unique opportunity for the UK and Europe to explore the surface of Mars, therefore all the instruments were designed to provide enough data to support as diverse a range of investigations as possible. Since the SCS team members could not be experts in all these different disciplines, we always envisaged making much the data available to the wider community for detailed analysis – consequently the SCS was presented at several US and European planetary conferences between 2001 and 2003 (e.g. Griffiths et al, 2002 & 2003a,b).

Furthermore, we knew that the mission would be extremely resource limited (i.e. power, bandwidth and the unknown mission lifetime in the hostile Martian environment). It was expected that once the DEM had been acquired and the lander location determined via stellar navigation, the search for geochemical evidence of extant or extinct Martian biology using the rest of the Beagle 2 instrument suite would rightly have a higher priority than further SCS imaging. Therefore, it was recognised that some of the science objectives below may have been unachievable due to mission resource limitations. With these considerations in mind, we established the following scientific objectives for the SCS system.

6.1 Panoramic colour imaging

Panoramic (360° azimuthal) colour imaging at 440, 530 and 670 nm would have been acquired early in the mission to help map and characterise the landing site and for public outreach purposes. Prior to landing, test

20

images were acquired with these filters and RGB images produced[4].

By acquiring extra visual band images with the L4 and R2 filters, the SCS team planned to use the method of Maki et al, (1999) to determine the CIE standard chromaticities of the Martian surface at Isidis. These chromaticities could be compared with "true colour" data from orbiters and other landing sites to provide high resolution, local information on the relative colour differences at different points on the planet's surface. We also planned to correct these images for ambient lighting effects, using data from night images acquired with the torch (see section 6.3). We would then be able to portray rock and soil surfaces as they would appear on Earth (i.e. under terrestrial solar illumination), providing geologists with extra visual information to help identify the rock surfaces under study.

Stereo pairs at 670 nm could also be acquired to extend the stereo mapping of the landing site beyond the PAW-arm workspace. Of course, our ability to map the landing site would degrade with distance due to nearby rocks obscuring the required lines of sight. Despite these potential gaps this DEM could be used to study the geomorphology, size distributions and area cover of rocks and boulders at the landing site. For example Bridges et al. (2003) estimated, based on data sets derived from Viking Lander images, that 5% of the landing site area was covered by rocks > 0.2 m high.

Due to its low elevation, the horizon for the SCS is calculated to be only 1.8 km from the lander (for a 1 m viewing height above a perfectly spherical Mars and assuming the necessary clear sight lines). However, given the spatial density of positive relief features in the part of the Mars Obiter Laser Altimeter DEM covered by the landing ellipse, Michael (2004) estimated a >70% probability of such features being recognised in the SCS panorama. In Isidis, potential landforms that might have been observed are crater walls and small knobs – judged from Mars Orbiter Camera images to resemble Icelandic pseudo cones 30–100 m tall (Bridges et al. 2003). SCS observations therefore, had the potential to yield useful data to confirm or refute the pseudo cone interpretation.

---

[4] (see SCS Website: http://www.mssl.ucl.ac.uk/www_plasma/missions/beagle2/beagle2.html)

6.2 Multi-spectral imaging of rocks and soils

Throughout the mission, further images would be acquired with the remaining nine geology filters to complete a multispectral panorama. Multi-spectral imaging of rocks and soils (from the panoramas or of individual high priority targets) provides information about their mineralogy and geochemistry from reflectance curves and colour ratios (e.g. McSween et al., 1999). This technique was used with great success by the PanCams on the twin NASA Mars Exploration Rovers (MERs – Bell et al., 2004). It would also be the only way (given Beagle 2's lack of mobility) of acquiring compositional information for parts of the landing site beyond the reach of the mole and robot arm. Additionally, as with the rock abrasion tool onboard each MER, a rock corer-grinder provided Beagle 2 with the capability to remove the dust and weathered surface layers to allow the SCS to image the unaltered rock material below.

Accurate radiometric calibration and solar-ambient sky illumination models are required to minimise the error in the determined surface reflectance values and hence any spectral and compositional data derived from them. Therefore, given the lack of precise QE data (see section 5.6) for the FM eyes the SCS radiometry would not have been as accurate as those achieved by recent missions. However, we planned to improve the quality of the illumination models using the torch (section 6.3) and hoped after the mission to calibrate the SCS reflectance spectra against GAP, Mössbauer and X-ray spectrometer geochemical analysis. An ultimate goal was to use this data set to provide ground truth to the Mars Express Omega spectrometer (Bibring et al., 2003).

6.3 Night observations using the torch

Observations of the surface near the lander were to be made at night using the torch (c.f. section 2) to determine the "true colour" of the surface materials, without the reddened component of sunlight scattered by dust particles during the day (e.g. Thomas et al., 1999). Initially, the camera would be calibrated on Mars by observing the calibration target illuminated by the torches at night and comparing it to the same measurements conducted on Earth prior to launch. Any changes in camera sensitivity with wavelength would then be used to update the camera spectral responsivity curves discussed in section 5.6. After this calibration, night images would be acquired of rock and soil surfaces near the lander, initially with the 440,

530 and 670 nm filters and then followed by the other nine geology filters as mission resources permitted.

Knowing the responsivity of the SCS and the spectral properties of the torches, we planned to determine the spectral radiance of the target materials and calculate the CIE standard chromaticities and therefore their appearance under any required illuminant (i.e. terrestrial sunlight). Comparison of the surface spectral properties observed in the day to those derived from night time imaging with the torch would allow us to constrain the spectral properties of direct solar and scattered components of the daytime illumination (at least at the time of day that the measurements were taken).

Additionally, the PLUTO instrument team suggested night observations of the hole left after the mole has been retrieved, to look for evidence of subsurface water sublimation at the bottom of the shaft and freezing out on the walls near the top of the shaft. Depending on sublimation rates and the minimum nightly temperature it is possible that some frost deposit may have been seen – however, no formal modelling was performed to estimate the likely quantity of water able to be mobilised along the mole shaft.

If mission resources had been available, the mole hole would almost certainly have been targeted to provide a view of the Martian subsurface. Due to the shadowing effect of the PAW, the torch would then have been required for illumination and it would have been logical (if speculative) to perform the imaging at night to investigate the PLUTO team's suggestion. Since the loss of Beagle 2, Mars Odyssey neutron spectrometer data (Feldman et al., 2004) has indicated that an upper limit of 4% of the material within a metre of the surface in Isidis is likely to be composed of ice.

6.4 Solar observations

Solar observations at 450, 670, 880 and 1000 nm were planned to measure the atmospheric optical density by direct comparison of the observed solar illumination with that expected for a clear atmosphere. Measurements of the variation of optical depth with time of year on Mars are required to improve our understanding of the Martian atmospheric physics due to the direct role of the dust in absorbing sunlight and heating the local atmosphere. This heating changes the atmospheric thermal profile and therefore

affects the formation of weather systems and growth and decay of both regional and rarer global dust storms. Additionally such information could be used to constrain the aerosol (dust and water ice) mean size and scattering properties (e.g. Smith and Lemmon, 1999). Optical density measurements are also important environmental data for the team operating the solar powered Beagle 2 lander.

Although local in extent, it was hoped that the optical density measurements would provide an important "ground truth" for the Mars Express instruments and simultaneous observations were planned early in the Beagle 2 mission. Optical depth measurements are also a prerequisite for determining the water vapour absorption, since the dust produces different extinction of the sunlight at the high solar zenith angles of interest (i.e. angles measured down from the zenith). Therefore, it is necessary to measure and deconvolve the dust optical density to accurately measure the water vapour signal.

Due to it's importance in the climatic, geological and biological evolution of Mars and because it is one of the most variable trace species in the present Martian atmosphere we were very interested in studying water vapour concentrations above Isidis during the Beagle 2 mission. Observations of the sun using the solar filters were planned to measure the relative depth of the 935 nm water vapour absorption line with respect to the nearby continuum (e.g. Titov et al., 1999). Clearly given the low abundance of water vapour near the Martian equator – typically < 20 precipitable microns – this is a very challenging task. However, by attempting these measurements at a range of zenith angles near the horizon (corresponding to different path lengths through the atmosphere and therefore different numbers of water vapour molecules), we proposed to constrain models of water vapour distribution with altitude.

In the months immediately prior to landing, collaboration had begun with colleagues at Oxford University, to model the variation of absorption with zenith angle for different water vapour distributions. We would then have attempted to fit these different possible models to the SCS absorption measurements. Unfortunately this work could not be carried out following the loss of Beagle 2. Therefore, we did not reach a position where we could confidently demonstrate that the SCS had sufficient sensitivity and signal to noise ratio to detect Martian water vapour over a useful zenith angle range.

6.5 Rock texture observations and Dust physical properties

Rock texture observations were planned at a working distance of 80 mm using the close-up lens (CUL). The CUL provides 60 micron resolution, intermediate between the 380 micron standard camera resolution and the 4 micron microscope resolution (Thomas et al., 2004). Blind tests, where geologists were shown standard DM RGB colour composite images of (previously unseen) rock samples, indicated that the accuracy of their photographic interpretations was greatly increased if (monochromatic) CUL pictures of the rock texture were also available.

The CUL might also have been used to observe the results of the Rock Corer Grinder's (Ng, 2003) attempts to remove the dust and weathered surface rind before a GAP sample is acquired. Also, images of lander surfaces, air bags, soil sample sites, mole shaft wall and landing scuffmarks in soil could in principle, be acquired with the microscope and CUL to help constrain the dust properties (e.g. Golombek et al., 1999).

6.6 Celestial navigation (and Phobos eclipse)

After landing but before Paw deployment from the lander base, we planned to image Phobos against the night sky to increase the accuracy of the determination of the landing site location on the surface of Mars. Trautner et al., (2003) determined that this celestial navigation technique can reduce the semi-major axis of the one-sigma landing error ellipse to as little as 8.5 km under ideal conditions (when it is limited by the accuracy of the knowledge of Phobos' orbit). Based on field trials at Observatorio de Sierra Nevada in Spain during the November 2002 ESA Leonid meteor observation campaign, the SCS can detect stars down to magnitude +3.5 using the 670 nm filters. At least two such "guide stars" (from approximately 200 with m > +3.5 visible in the entire sky) are required for this technique to work. Therefore, there would be typically up to eight stars to chose from in each 48° field-of-view SCS image of Phobos, and up to two attempts to image Phobos on each of the first three nights after landing.

Once the landing site position has been determined to this level of precision, the Mars Express High Resolution Stereo Camera (HRSC – Neukum and the HRSC team, 2003) would have been able to produce

a DEM of the area of the revised landing ellipse. Matching of topographical highs in this DEM with landmarks in the SCS panoramas could yield a Beagle 2 location accurate to several metres (Neukum, 2003).

6.7 Other Possible Targets of Opportunity

Other possible observations included multi-spectral imaging of Phobos & Deimos (a maximum of ~ 5 and 0.8 pixels in diameter respectively) with the geology filters to measure their spectral reflectance curve and attempting to image the Earth (calculated diameter of 0.13 pixels at its closest at the beginning of the mission) for public outreach purposes. In addition, transitory or seasonal changes (dust accumulation, surface frosts) at the landing site or in the sky above it (dust devils, clouds and possibly even meteors) might have been observed.

The DM SCS observed meteors successfully on Earth under manual control during the ESA Leonid campaign and some thought was given to observing them on Mars (Christou & Beurle, 1999). However given the mission operations constraints, 65 second integration time limit and a lack of an onboard software comparator to detect and save potential meteor images, in practice the SCS would have been extremely unlikely to have captured an image of a Martian meteor during the few night time images that were planned for landing site location.

7. Conclusions

This paper has provided an introduction to the design of the Stereo Camera System, the choice of filter wavelengths and a description of the primary engineering goal of generating a DEM of the landing site within reach of the PAW. A review of the basic calibration programme that the flight models underwent before launch and the flight image calibration software was included. Finally, a discussion of the major scientific objectives of the SCS on Mars was provided.

The SCS was designed to return stereoscopic and colour images at 440, 530 and 670 nm, and multispectral

panoramic images at twelve wavelengths from 440 to 1000 nm. Additionally six solar filters were included to measure the absorption of sunlight by water vapour and suspended dust particles. A close-up lens and wide-angle mirror extended the SCS's capabilities – while a pair of torches provided for the first time the possibility of observing the Martian surface adjacent to the lander under known illumination conditions.

Although it returned no data from the surface of Mars due to the loss of Beagle 2 on landing, the SCS team have a designed, built and calibrated a 360 g stereo multispectral imager capable of returning high resolution colour panoramic images from a variety of inner solar system targets. It is hoped that these lightweight and versatile cameras will achieve greater success on future flight opportunities. Indeed the SCS team is part of an enlarged camera team contributing to the Pasteur payload on the ExoMars rover for the proposed ESA Aurora programme.

References

Barabash, S., Lundin, R., Andersson, H., Gimholt, J., Holmström, M., Norberg, O., Yamauchi, M., Asamura, K., Coates, A.J., Linder, D.R., Kataria, D.O., Curtis, C.C., Hsieh K.C., Sandel, B.R., Fedorov, A., Grigoriev A., Budnik, E., Grande, M., Carter, M., Reading, D.H., Koskinen, H., Kallio, E., Riihela, P., Säles, T., Kozyra, J., Krupp, N., Livi, S., Woch, J., Luhmann, J., McKenna-Lawlor, S.,

Orsini, S., Cerulli-Irelli, R., Mura, A., Milillo, A., Roelof, E., Williams, D., Sauvaud, J.-A., Thocaven, J.-J., Winningham, D., Frahm, R., Scherrer, J., Sharber J., Wurz, P. and Bochsler, P., 2002, ASPERA-3: Analyser of Space Plasmas and Energetic Ions for Mars Express, ESA Special Publication, SP-1240.

Barnes, D., Taylor, E., Phillips, N., Gossant, A., Paar, G, Sims, M. and Pullan, D., 2002, Beagle2 arm and PAW SCS calibration: Preliminary results, Beagle 2 project internal report issued by the University of Aberystwyth.

Barnes, D.P., Phillips, N., and Parr, G., 2003, Beagle2 Simulation and Calibration for Ground Segment Operations. 7th International Symposium on Artificial Intelligence, Robotics and Automation in Space (i-SAIRAS), 2003, Japan. CD-ROM proceedings.

Bell III, J.F., et al., 2003, Mars Exploration Rover Athena Panoramic Camera (Pancam) investigation, *J. Geophys. Res.,* **108** (E12), 8063–8092, Nov. 29, 2003.

Bell III, J.F., et al., 2004, Pancam Multispectral Imaging Results from the Opportunity Rover at Meridiani Planum, *Science*, **306**, 1703–1709, Dec. 3, 2004

Bertaux, J.L., Guibert, S., Korablev, O., and the SPICAM Team, 2002, SPICAM on Mars Express: The atmosphere of Mars from top to bottom, in abstracts of the Mars atmosphere modelling and observations workshop, Granada, Spain, 13-15 January 2002.

Bibring, J.P., Gondet, B. and Langevin, Y., 2003, Observation strategies for the OMEGA imaging spectrometer on-board Mars Express, *Geophys. Res. Abs.*, **5**, 09389, 2003

Bridges, J.C., et al., 2003, Selection of the landing site in Isidis Planitia of Mars probe Beagle 2, *J. Geophys. Res.,* **108** (E1), 5001–5017, Jan. 25, 2003.

Christou, A.A., & Beurle, K., 1999, Meteoroid streams at Mars: possibilities and implications, *Planet. Space Sci.*, **47**, 12, 1475–1485, Dec. 1999

Christou, A.A., 2002, Lander position determination on Mars using Phobos transits: application to Beagle 2, *Planet. Space Sci.*, **50**, 7–8, 781–788, Jun.-Jul. 2002

Feldman, W. C., et al., 2004, Global distribution of near-surface hydrogen on Mars, *J. Geophys. Res.*, **109**, E09006, doi:10.1029/2003JE002160.

Formisano, V. and the PFS team, 2001, An integrated approach to the study of Mars with the Planetary Fourier Spectrometer, *Geophys. Res. Abs.*, **3**, 07253, 2001.

Golombek, M.P., et al., 1999, Overview of the Mars Pathfinder Mission: Launch through landing, surface operations, data sets, and science results, *J. Geophys. Res.,* **104** (E4), 8523–8553, Apr. 25, 1999.

Griffiths, A.D., Coates, A.J., Josset, J-L., Paar, G. and Sims, M.R., 2003, The Beagle 2 Stereo Camera System, LPSC XXXIV, Abstract #1609, Houston, Mar. 17-21, 2003a.

Griffiths, A.D., Coates, A.J., Josset, J-L., Paar, G. and Sims, M.R., 2003, The Beagle 2 Stereo Camera System, Geophys. Res. Abs., 5, 07371, 2003b.

Griffiths, A.D., Coates, A.J., Howett, C. and Knowelden, R., 2002, Dust Removal Techniques for the Beagle 2 Stereo Camera System External Optics, LPSC XXXIII, Abstract#1012, Houston, Mar. 11-15, 2002.

Janesick, J.R., 2001, Scientific Charge-Coupled Devices, SPIE Press, 2001

Josset J.-L. and Beauvivre, S. , 2003, High-Performances Micro-Cameras of the Mars Express Lander, *Geophys. Res. Abs.*, **5**, 14329, 2003.

Maki, J.N., Lorre, J.J., Smith, P.H., Brandt, R.D., Steinwand, D.J., 1999, The colour of Mars: Spectrophotometric measurements at the Pathfinder landing site, *J. Geophys. Res.,* **104** (E4), 8781–8794, Apr. 25, 1999.

McSween, Jr., H.Y., et al., 1999, Chemical, multispectral, and textural constraints on the composition and origin of rocks at the Mars Pathfinder landing site, *J. Geophys. Res.,* **104** (E4), 8679–8715, Apr. 25, 1999.

Michael, G.G., 2004, Beagle-2 position determination from the returned camera panoramas using MOLA data, *Planet. Space Sci.*, **52**, 4, 271 – 277, Mar. 2004

Morgan, G.H., et al., 2003, The Gas Analysis Package on the Beagle 2 Lander, *Geophys. Res. Abs.*, **5**, 09891, 2003

Neukum, G., 2003, personal communication.

Neukum, G. and the HRSC team, 2003, The High Resolution Stereo Camera (HRSC) Experiment onboard the European Mars Express (MEX) Mission, *Geophys. Res. Abs.*, **5**, 07371, 2003.

Ng, T.C., et al., 2003, First planetary rock coring in our solar system ESA 2003 Beagle 2 Mars mission, *LPSC XXXIV*, Abstract #1002, Houston, Mar. 17-21, 2003.

Paar, G., Bauer, A. and Sidla, O., 1999, Near range stereo for Mars landing site reconstruction, Proc. SPIE

3827, 22 Industrial Lasers and Inspection, Munich, Jun. 14-17, 1999.

Pillinger, C.T., (with Sims, M.R. and Clemmet, J.), 2003. The Guide to Beagle 2 (Produced & published by C.T. Pillinger as a contribution to Open University short course S198 *Exploring Mars: Beagle 2 and the search for life*, December 2003).

Rueffer, P., Borrmann, A., Versatile Image Data Compression For The Beagle 2 Probe, IEEE International Geoscience and Remote Sensing Symposium (IEEE IGARSS 2003), Toulouse, July 2003.

Sims, M.R., Pillinger, C.T., Wright, I.P., Morgan, G., Fraser, G., Pullan, D., Whitehead, S., Cole, R., Wells, A., Richter, L., Kochan, H., Hamacher, H., Johnstone, A., Coates, A., Peskett, S., Brack, A., Clemmet, J., Slade, R., Phillips, N., Berry, C., Senior, A., Lingard, J.S., Underwood, J.C., Zarnecki, J., Towner, M., Leese, M., Gambier-Parry, A., Thomas, N., Josset, J.L. and Klingelhofer, G., 1999, Beagle 2: The Exo-Biology Lander for ESA's 2003 Mars Express Mission, Proc. SPIE **3755**, 10–23.

Sims, M.R., Pillinger, C.T., Wright, I.P., Morgan, G., Praine, I.J., Fraser, G., Pullan, D., Whitehead, S., Dowson, J., Wells, A., Richter, L., Kochan, H., Hamacher, H., Griffiths, A., Coates, A., Peskett, S., Brack, A., Clemmet, J., Slade, R., Phillips, N., Berry, C., Senior, A., Zarnecki, J., Towner, M., Leese, M., Zent, A., Thomas, N., Josset, J.L., Klingelhofer, G., van Duijn, P. and Sims, G., 2000, Instrumentation on Beagle 2: The Astro-Biology Lander on ESA's 2003 Mars Express Mission, Proc. SPIE **4137**, 36–47.

Sims, M.R., Pullan, D., Fraser, G.W., Whitehead, S., Sykes, J., Holt, J., Butcher, G., Nelms, N., Dowson, J., Ross, D., Bicknell, C., Crocker, M., Favill, B., Wells, A., Richter, L., Kochan, H., Hamacher, H., Ratke, L., Griffiths, A., Coates, A., Phillips, N., Senior, A., Zarnecki, J., Towner, M., Leese, M., Patel, M., Wilson, C., Thomas, N., Hviid, S., Josset, J.L., Klingelhofer, G., Bernhardt, B., van Duijn, P., Sims, G. and Yung, K.L., 2003, Performance Characteristics of the PAW Instrumentation on Beagle 2 (The Astrobiology Lander on ESA's Mars Express Mission), Proc. SPIE **4859**, 32–44.

Smith, P.H., et al., 1997a, The imager for Mars Pathfinder experiment, *J. Geophys. Res.,* **102** (E2), 4003–4025, Feb. 25, 1997.

Smith, P.H., et al., 1997b, Results from the Mars Pathfinder Camera, *Science*, **278**, 1758–1764, Dec. 5, 1997

Smith, P.H. and Lemmon, M., 1999, Opacity of the Martian atmosphere measured by the Imager for Mars

Pathfinder, *J. Geophys. Res.,* **104** (E4), 8975–8985, Apr. 25, 1999.

Smith, P.H., Reynolds, R., Weinberg, J., Friedman, T., Lemmon, M.T., Tanner, R., Reid, R.J., Marcialis, R.L. Bos, B.J. and Oquest, C., 2001, The MVACS Surface Stereo Imager on Mars Polar Lander, *J. Geophys. Res.,* **106** (E8), 17,589 –17,607, Aug. 25, 2001.

Squyres, S.W., et al, 2004, The Spirit Rover's Athena Science Investigation at Gusev Crater, Mars, *Science*, **305**, 794–799, Aug. 6, 2004

Thomas, N., Markiewicz, W.J., Sablotny, R.M., Wuttke, M.W., Keller, H.U., Johnson, J.R., Reid, R.J. and Smith, P.H., 1999, The color of the Martian sky and its influence on the illumination of the Martian surface, *J. Geophys. Res.,* **104** (E4), 8795-8808, Apr. 25, 1999.

Thomas, N., Lüthi, B.S., Hviid, S.F., Keller, H.U., Markiewicz, W.J., Blümchen, T., Basilevsky, A.T., Smith, P.H., Tanner, R., Oquest, C., Reynolds, R., Josset, J.-L., Beauvivre, S., Hofmann, B., Rüffer, P., Pillinger, C.T., 2004, The microscope for Beagle 2, Planet. Space Sci., 52, 9, 853–866, Aug. 2004.

Titov, D.V., et al., 1999, Measurements of the atmospheric water vapour on Mars by the Imager for Mars Pathfinder, *J. Geophys. Res.,* **104** (E4), 9019–9026, Apr. 25, 1999.

Trautner, R., Manaud, N., Michael, G., Koschny, D., Griffiths, A., Coates, A., Josset, J-L., Beauvivre, S., 2004. Determination of the Beagle2 Landing Site, Proceedings of International Workshop on Planetary Probe Atmospheric Entry and Descent Trajectory Analysis and Science, 6–9 October 2003, Lisbon, Portugal, ESA SP544, 175–181, 2004.

Figure 1: The position of the flight model stereo cameras, wide-angle mirror (stowed position) and torches on the Beagle 2 PAW. By convention (with the PAW orientated so that the robot arm "wrist" joint is above the cameras), the terms left and right are analogous to the eyes of an observer viewing the same scene.

Figure 2: An exploded view of the CAD model of one of the Stereo Camera System "eyes" (the eyes are identical except for their filter characteristics).

Figure 3: Laboratory test image from the development model camera showing the performance of the 48° optics in the 0.6–1.2 m short focus range. The telephone is approximately 1 m from the camera.

Figure 4: A typical close-up lens image of a rock specimen, acquired during SCS testing. A tape measure with centimetre (top) and inch (bottom) markings is included for scale. Image depth of field is approximately 1 cm.

Figure 5: A wide-angle mirror (WAM) image (with the torch illuminated), acquired during lander verification. The WAM was to be used in this configuration to acquire the first image shortly after landing on Isidis Planitia. The lander base occupies the central 43% of the illuminated image area.

Figure 6: The spectrum of the 'ultra-bright' white LEDs used for the torches (from manufacturer's data).

Figure 7: Flight model CCD transfer curves for both the left and right eyes. Linear fits (straight lines) are shown with corresponding equations and correlation coefficients.

Figure 8: Flight model CCD linearity curves for both the left and right eyes. Linear fits (straight lines) are shown with corresponding equations and correlation coefficients.

Figure 9: Development model CCD quantum efficiency measurements (circles) compared with manufacturer's data (solid line). Error bars include an estimated 10% error on the photometer

measurements.

Figure 10: Graphical comparison of responsivity versus wavelength for three recent Mars-lander imaging systems: the MVACS Surface Stereo Imager, the Mars Exploration Rover-A (Spirit) PanCam and the Beagle 2 SCS. Horizontal error bars are used to illustrate the filter band passes (full width-half maximum values).

Figure 11: Signal to Noise ratios for the left and right eyes at 25 °C (calculated using manufacturer's quantum efficiency data and assuming a maximum signal level of 800 DN after a 10 second integration).

Figure 12a: Plot of brightness profiles across three images of a 21 micron width slit acquired with the Left eye #7 filter (separation is ~0.7 m). The three perpendicular profiles are for the slit oriented horizontally, vertically and diagonally (45°) to the CCD pixel row structure. b: Comparison of Modulation Transfer Function (MTF) plots for the L7 filter viewing the slit oriented horizontally, vertically and diagonally. Note, vertical and diagonal slit MTFs are closely comparable.

Figure 13: Plot of MTF against spatial frequency for selected plane parallel filters, lenticular filters and the CUL (object distances are ~0.7, ~1.3 and 0.08 m respectively). MTF ranges from 38% to 3% at the Nyquist frequency of 34.7 mm^{-1} (where the curves terminate). The legend indicates the filter wavelength, name and the slit orientation (90° = vertical and 45° = diagonal) relative to the CCD pixel row structure.

Parameter	FM-1 (Left) and/or FM-2 (Right)	
Dark figure of merit [nA/cm^2]	0.70 ± 0.07	0.84 ± 0.79
Read out noise [electrons]	292 ± 26	257 ± 22
Full well [electrons]	$811 \pm 0.90 \times 10^3$	$679 \pm 0.82 \times 10^3$
Gain [electrons/DN]	792 ± 21	663 ± 16
Signal to Noise Ratio	141 ± 59	122 ± 52
Exposure time [ms]	1–65535 (in 1 ms steps)	
Frame transfer [ms]	2	
Readout time [ms]	1132	
Spectral range [nm]	440–1000	
A/D Conversion [bits/pixel]	10	
Number of Pixels	1024 x 1024	
Pixel Size [µm]	14 x 14	

Table 1: Typical s CCD characteristics

Parameter	Flat and/or Lenticular filters	
Focal length, f [mm]	22.26	22.71
Focal Ratio	f/11.13	f/11.35
Minimum focus [a] [m]	0.6	1.2
Maximum focus [a] [m]	1.2	infinity
Toe-in angle [°]	3.73	
Stereo Baseline [mm]	209	
Field of View [°]	48 (illuminated max.)	
	34 (along CCD edge)	
FOV 100% Overlap [m]	1.2	
Scale [mrad/pixel]	0.75	

[a] Distance for sharp focus over entire field of view.

Table 2: Stereo camera system optical characteristics

Filter #[a]	CW[b] (nm)	PB[c] (nm)	Type	Filter #[a]	CW[b] (nm)	PB[c] (nm)	Type
L1[e]	481	28	Geology	R1[e]	720	560	CUL[d]
L2	439	22	Geology	R2	602	21	Geology
L3	532	32	Geology	R3	799	20	Geology
L4	750	18	Geology	R4	906	42	Geology
L5	857	34	Geology	R5	961	29	Geology
L6	930	32	Geology	R6	1003	28	Geology
L7	669	17	Geology/DEM	R7	668	17	DEM
L8	671	17	Far Stereo	R8	668	18	Far Stereo
L9	928	5.5	Solar	R9	440	22	Far Colour
L10	936	5.6	Solar	R10	532	32	Far Colour
L11	1000	6	Solar	R11	449	4	Solar
L12[f]	877	6	Solar	R12[f]	670	5.5	Solar

[a] filter wheel location (L = left or FM-1, R = right or FM-2 camera);
[b] CW = centre wavelength; [c] PB = pass band;
[d] CUL = close-up lens (working distance is 8–9 cm),
[e] selecting this filter causes the wiper to pass across the front window;
[f] filter wheel reference home position.

Table 3: The complete stereo camera system filter set.

Filter #[a]	CW[b] [nm]	PB[c] [nm]	Comments (see tables 3 & 4 in Smith, et al. 1997)
L1	481	28	Discriminate crystalline hematite, crystalline goethite, & nanophase ferric oxide
L2	439	22	Blue; Ferric oxides/oxyhydrides
L3	532	32	Green; hematite, d-FeOOH, goethite & lepidocrocite
L4	750	18	Ferric oxides (local max.) oxyhydroxide minerals
L5	857	34	Hematite, Pyroxines & Olivines
L6	930	32	Low-Ca clinopyroxines
R2	602	21	Ferric oxyhydroxide (local max.)
R3	799	20	Maghemite (local max.)
R4	906	42	Goethite, enstatite & hypersthene
R5	961	29	Ferrous silicates
R6	1003	28	Diopside & fosterite
R7	668	17	Ferric oxides/oxyhydrides & Iron Silicates & Near Stereo

[a] filter wheel location (L = left or FM-1, R = right or FM-2 camera);
[b] CW = centre wavelength; [c] PB = pass band.

Table 4: Stereo camera system geology filter set.

Filter Position	Centre Wavelength [nm]	Filter Band pass [nm]	Total System Transmission	Quantum Efficiency [a]	System Gain [e⁻/DN]	Responsivity [b] [(DN/s)/(W/ (m².sr.µm))]
L1	481.0	28.0	0.718	7.41%	792	34.30
L2	438.8	21.6	0.638	3.51%	792	10.17
L3	532.0	32.0	0.695	10.86%	792	61.56
L4	750.0	18.0	0.713	15.84%	792	72.95
L5	857.0	34.0	0.799	10.54%	792	117.47
L6	930.0	32.0	0.721	6.39%	792	65.66
L7	669.0	17.2	0.701	18.27%	792	70.54
L8	671.0	17.2	0.689	18.20%	792	69.29
L9	928.0	5.5	3.93×10^{-4}	6.51%	792	6.25×10^{-3}
L10	936.0	5.6	2.52×10^{-4}	6.00%	792	3.80×10^{-3}
L11	999.8	6.0	5.02×10^{-4}	2.87%	792	4.14×10^{-3}
L12	877.3	6.0	3.58×10^{-4}	9.26%	792	8.37×10^{-3}
R1	*720.0*	*560.0*	*0.637*	*11.15%*	*663*	*1637.61*
R2	601.5	21.0	0.663	13.22%	663	63.35
R3	799.0	20.0	0.728	14.11%	663	93.85
R4	906.0	42.0	0.792	7.28%	663	125.51
R5	960.5	29.0	0.733	4.66%	663	54.44
R6	1003.0	28.0	0.735	2.68%	663	31.64
R7	668.0	17.2	0.703	18.14%	663	83.77
R8	668.0	18.0	0.682	18.14%	663	85.10
R9	440.3	22.2	0.594	3.64%	663	12.09
R10	532.0	32.0	0.684	10.92%	663	72.71
R11	449.0	4.0	3.21×10^{-4}	4.41%	663	1.45×10^{-3}
R12	669.8	5.5	3.64×10^{-4}	18.27%	663	1.40×10^{-2}

[a] Manufacturer's data at 25°C; [b] Calculated for 25°C from QE data

Table 5: Calculated stereo camera system responsivity, with quantum efficiency and total transmission for the complete filter set. The values for the wideband close-up lens responsivity & transmission (*italic*) are upper limits.
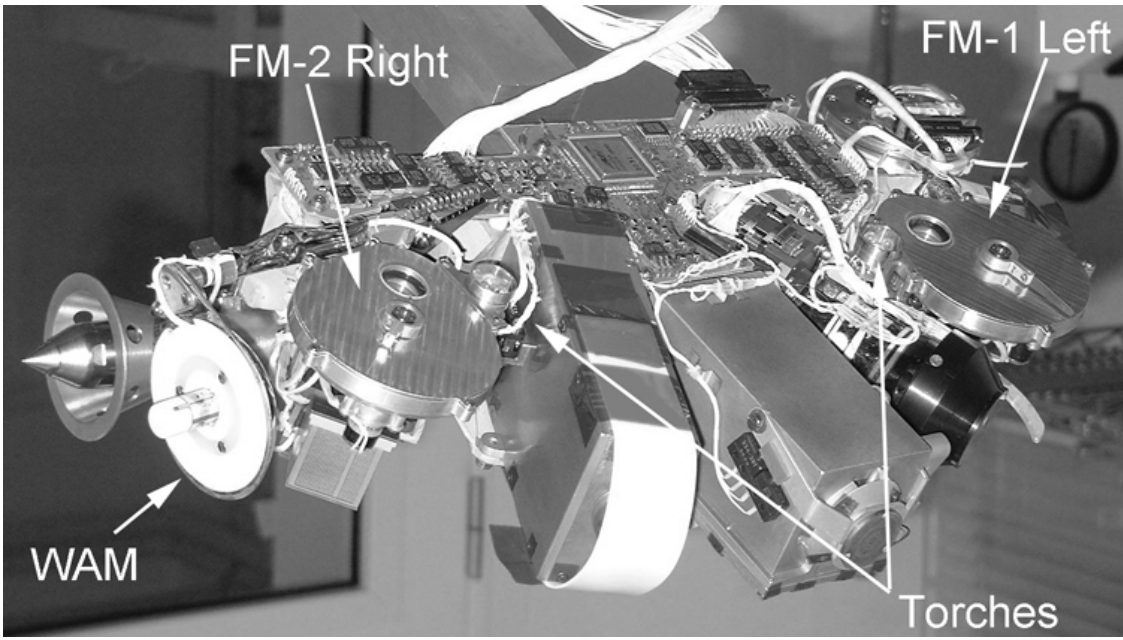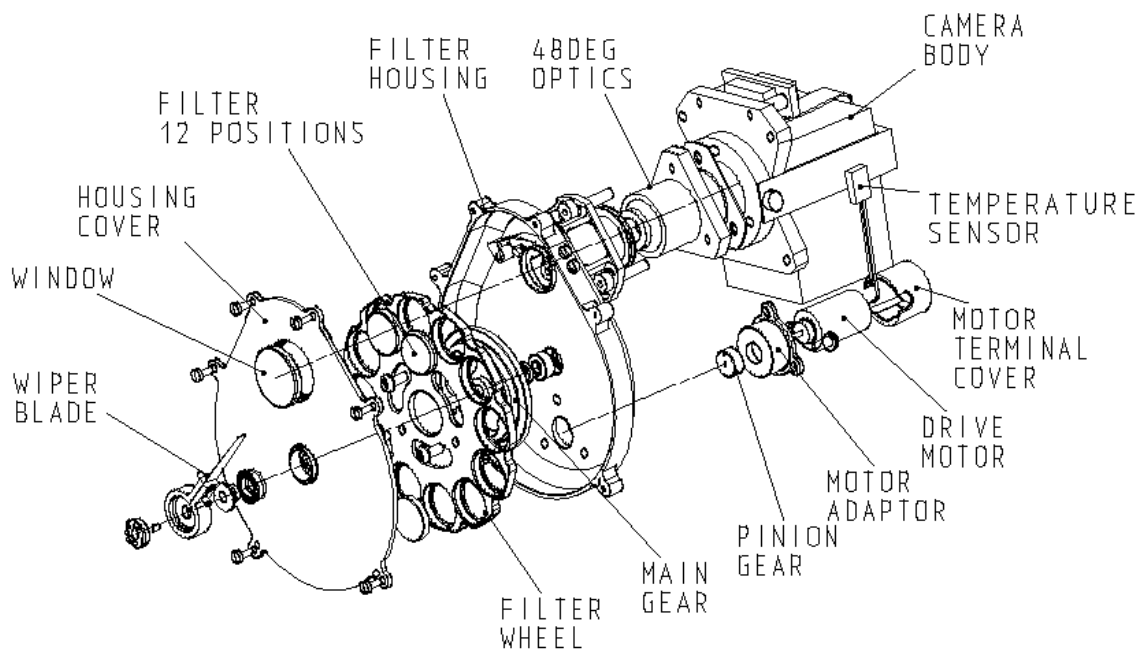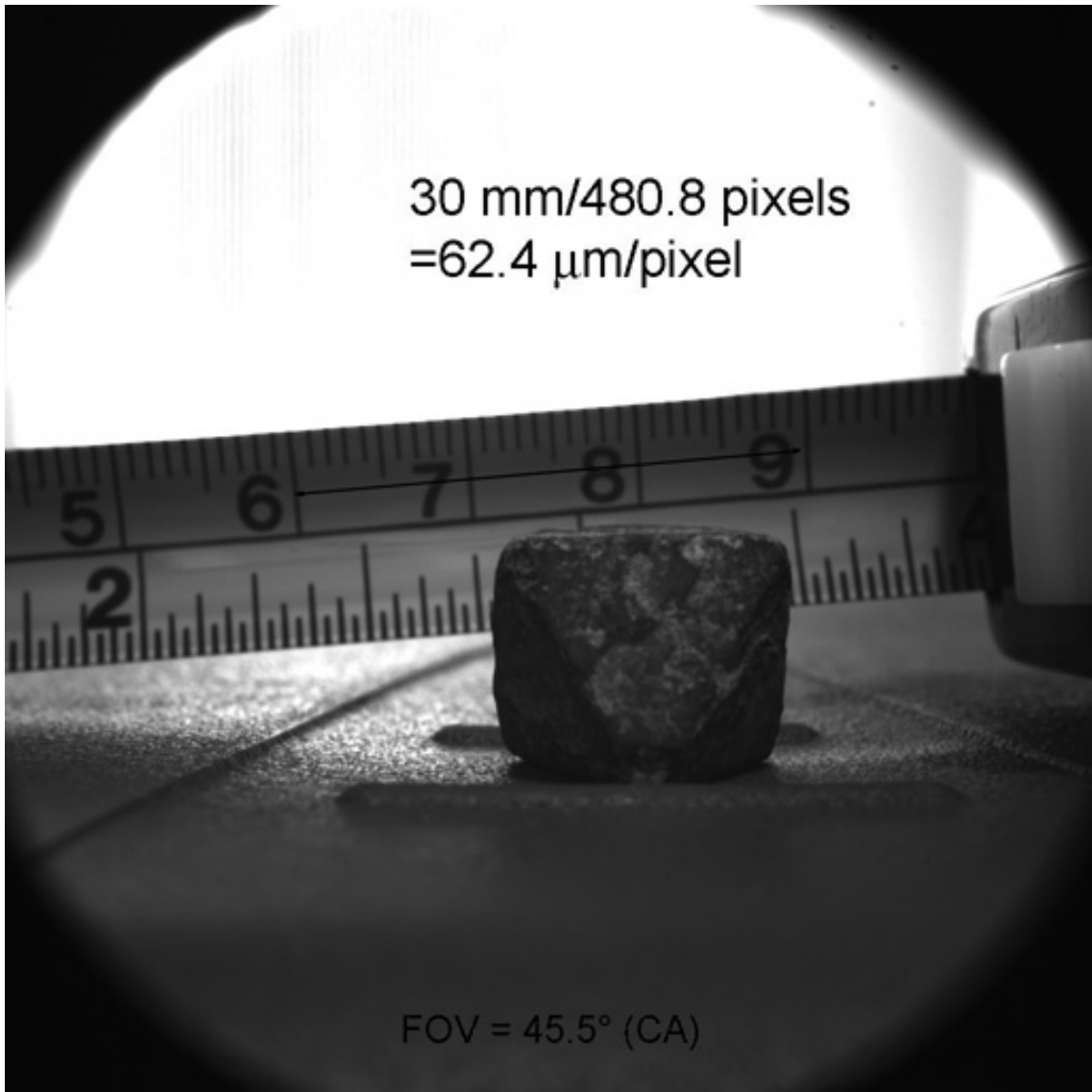
Figure 1
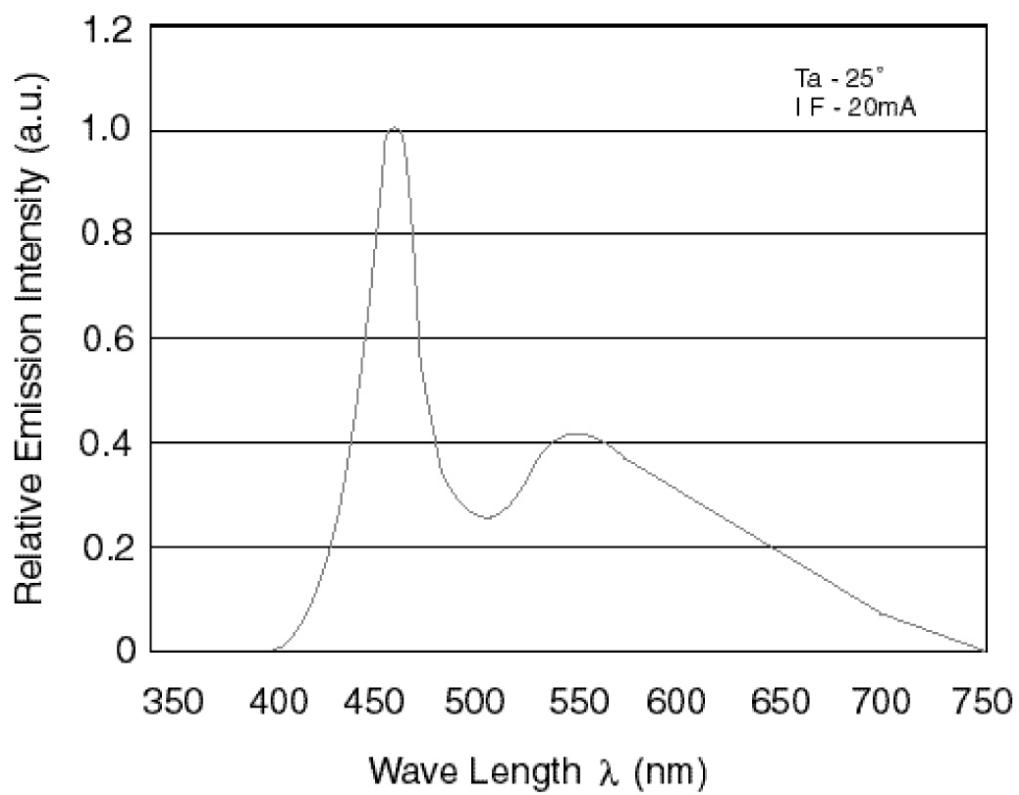
Figure 2

Figure 3

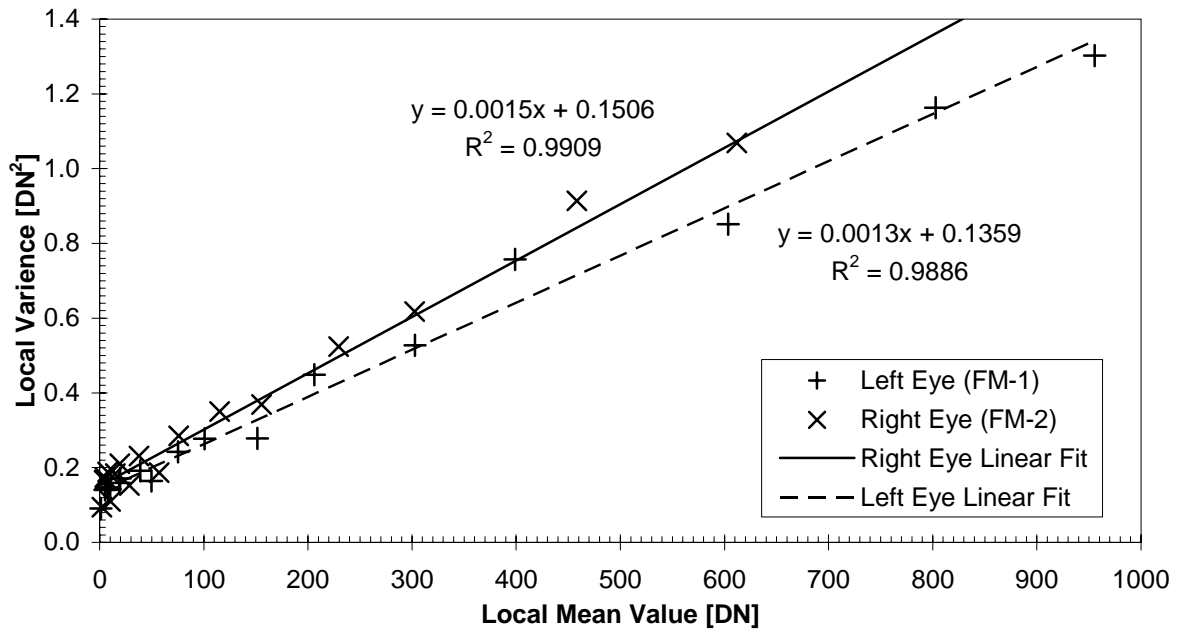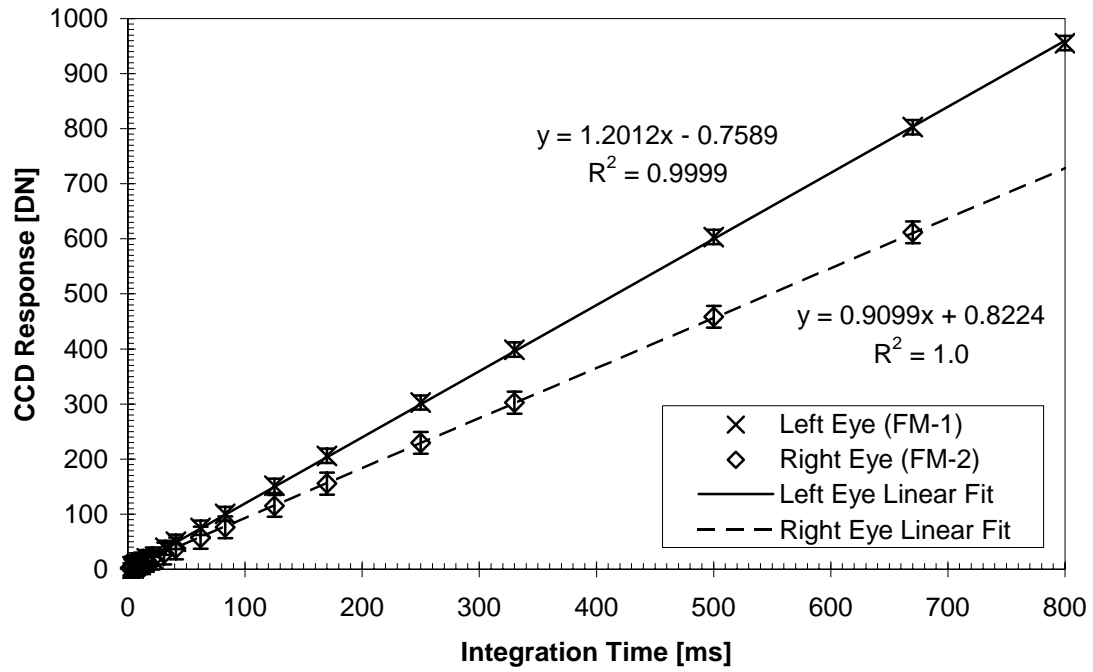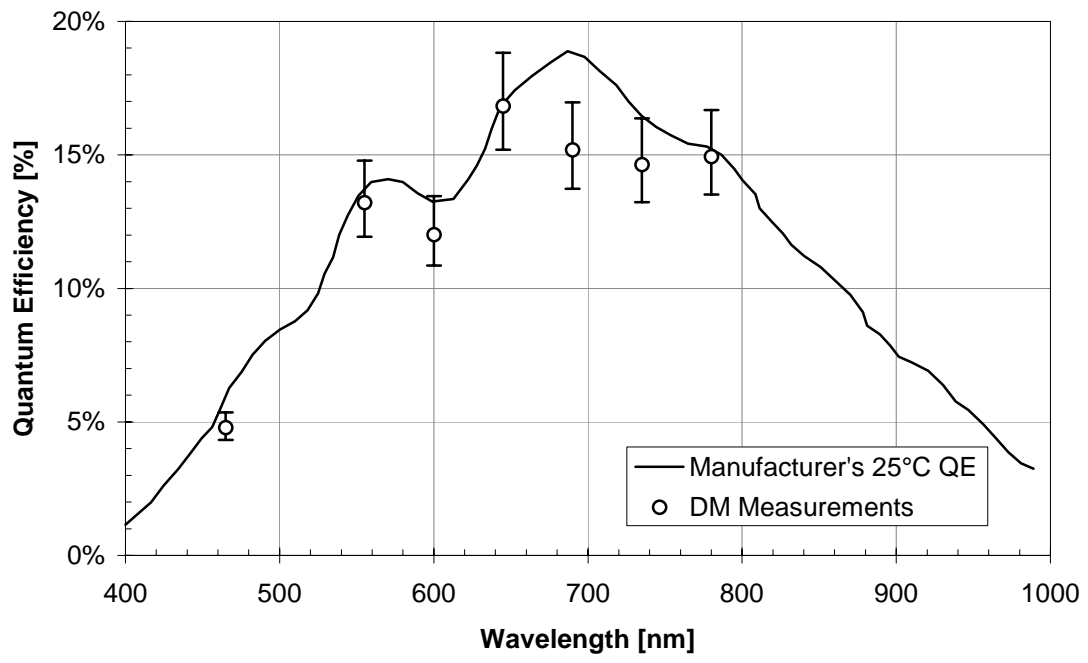30 mm/480.8 pixels
=62.4 μm/pixel

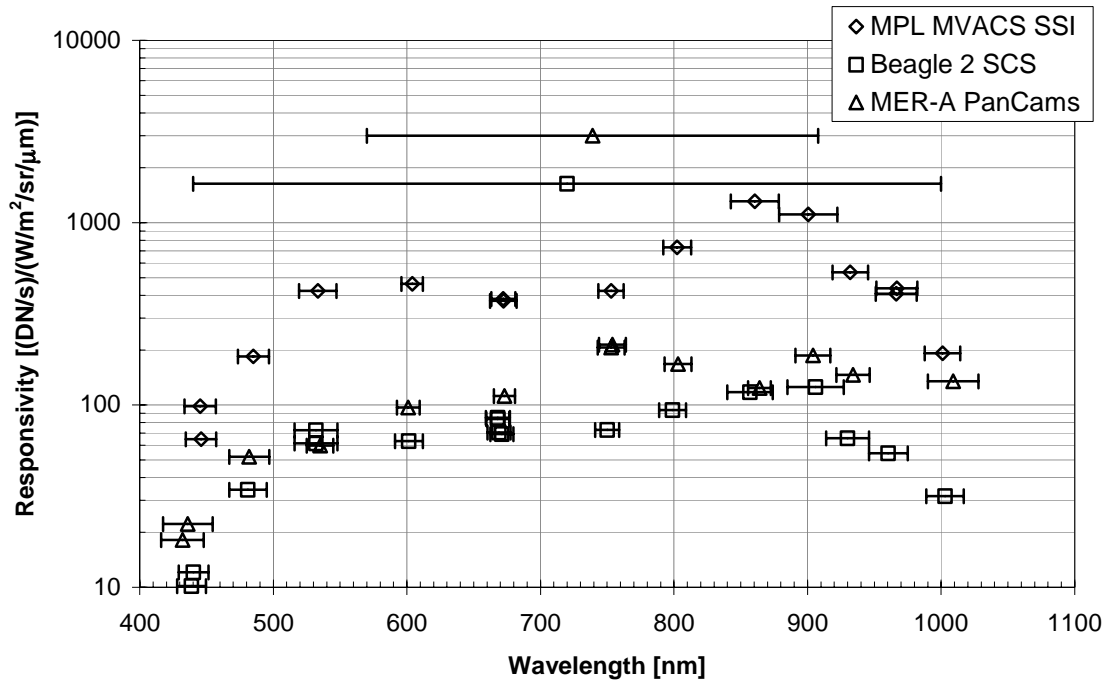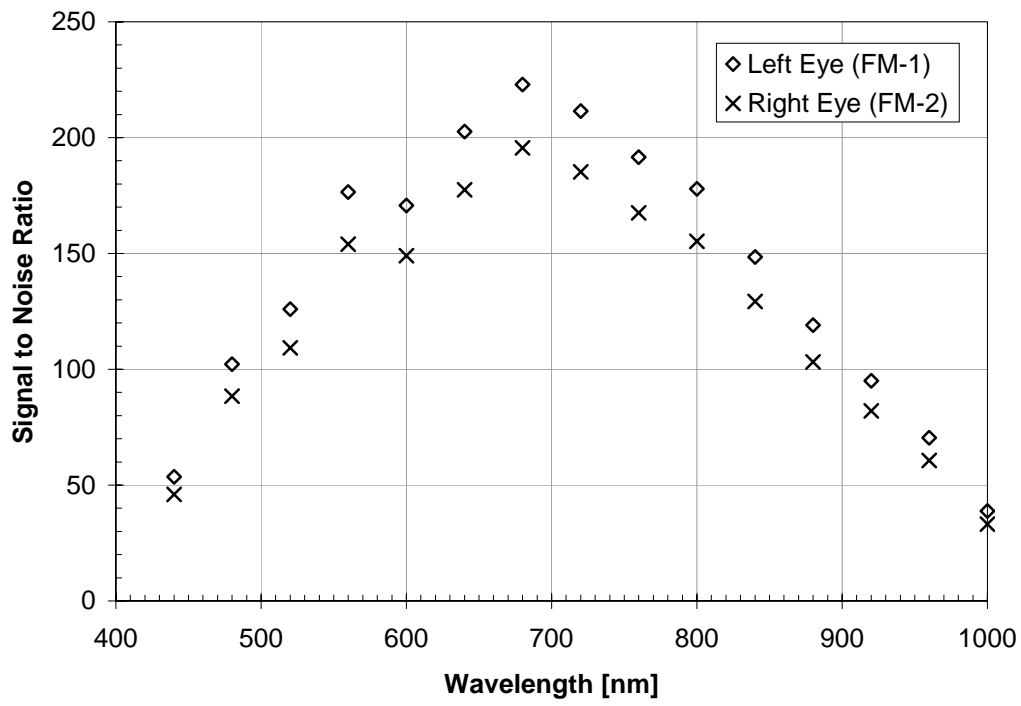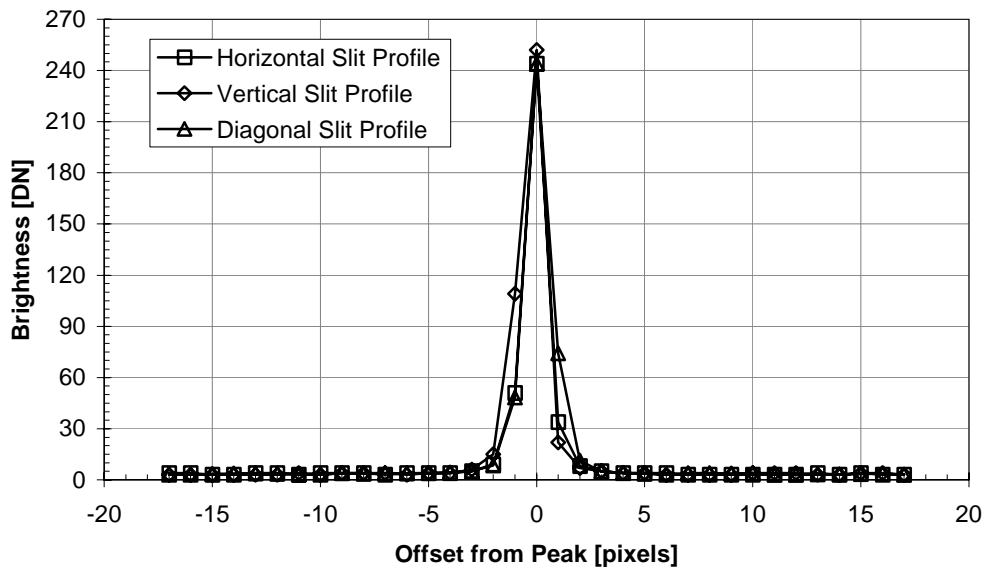FOV = 45.5° (CA)
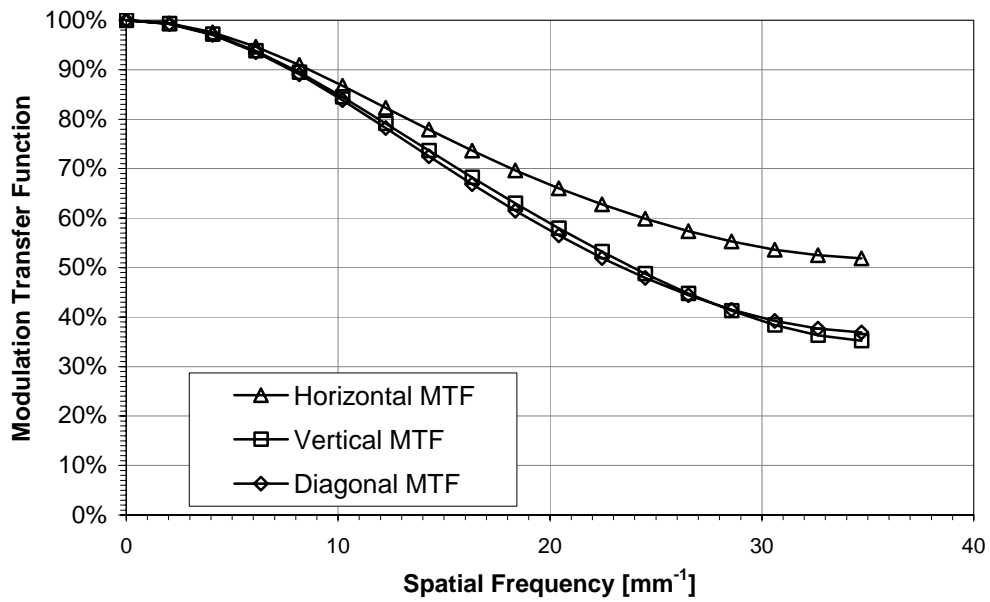
Figure 4

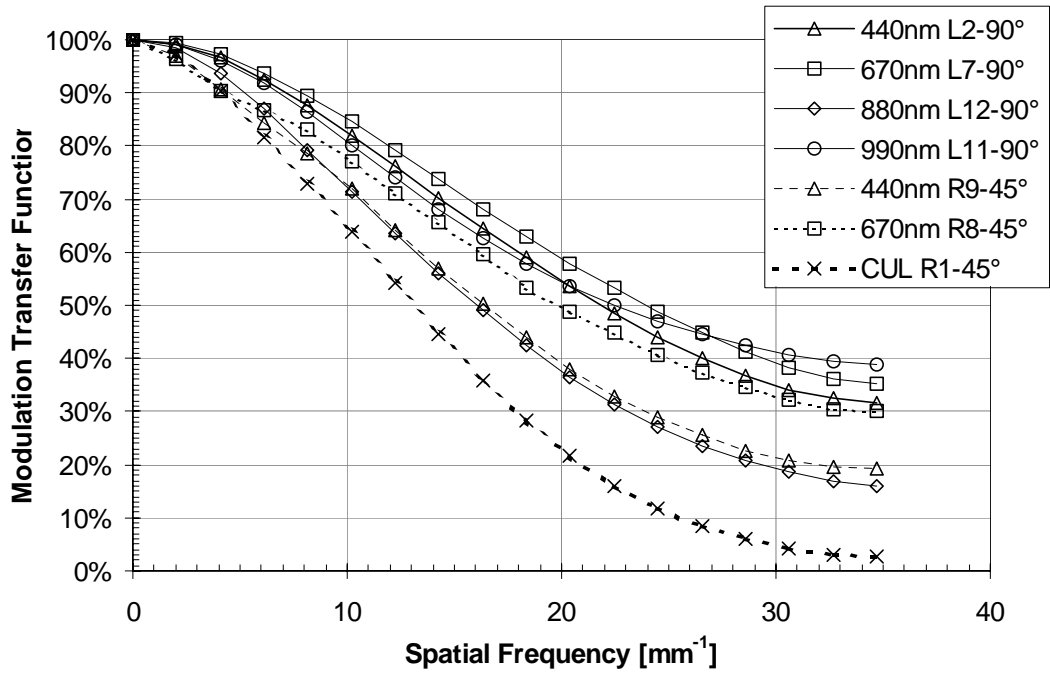Figure 5

Figure 6

Figure 7

Figure 8

Figure 9

Figure 10

Figure 11

Figure 12a

Figure 12b

Figure 13